4-2002

Motion of Droplets Along Thin Fibers With Temperature Gradient

Alexander L. Yarin

Wenxia Liu
University of Akron Main Campus

Darrell Hyson Reneker
University of Akron Main Campus, reneker@uakron.edu

Motion of droplets along thin fibers with temperature gradient

Alexander L. Yarin
Faculty of Mechanical Engineering, Technion, Haifa 32000, Israel

Wenxia Liu and Darrell H. Reneker
Maurice Morton Institute of Polymer Science, The University of Akron, Ohio 44325-3909

(Received 7 June 2001; accepted for publication 21 January 2002)

Liquid *n*-decane, *n*-undecane, *n*-dodecane, and *n*-hexadecane formed tiny symmetrical droplets on a partially wettable cylindrical fiber. When a temperature gradient was created along the fiber, the droplets began to move along the fiber toward the cold region. An explanation of the phenomenon is related to the thermocapillary motion. Other possible mechanisms were ruled out. The theoretical results and experimental data agree reasonably well. © *2002 American Institute of Physics.* [DOI: 10.1063/1.1459099]

I. INTRODUCTION

Small droplets deposited on a partially wettable cylindrical fiber are axisymmetric.[1] In the present experiments it was found that when a temperature gradient was created along a thin horizontal fiber, droplets moved toward the cold region. Description of the experimental findings and theoretical modeling are the main aims of the present work. Motion of tiny droplets and bubbles driven by temperature gradients is typically related to the thermocapillary Marangoni convection.[2,3] Thermal Marangoni effects result from surface tension changes, typically reduction of surface tension as temperature increases. In the experiments of Ref. 2, as well as in a number of works discussed in Ref. 3, it was shown that droplets and bubbles move toward the *hotter regions*. On the other hand, motion of thin liquid films, which may be considered as two-dimensional drops, toward the *colder regions* demonstrated in Refs. 4 and 5 was also attributed to the thermocapillary Marangoni convection. The resolution of this paradox is related, from our point of view, to the fact that in Refs. 2 and 3 moving droplets or bubbles were fully submerged in a confined solvent so that counterflows are significant, whereas in Refs. 4 and 5 the moving films were actually free from counterflows. In all four cases thermocapillary Marangoni stresses acting over the droplet or bubble interface pulled liquid toward the cold region. In the case of thin free liquid films[4,5] these stresses pulled the entire film toward the cold region. In the experiments of Ref. 2, when solvent about a bubble was pulled toward the cold region, a counterflow must have occurred in the incompressible fluid due to the effect of the confinement. The counterflow was actually responsible for the bubble motion toward the hot region. Confined and free are terms used to distinguish situations in which the counterflow of a surrounding fluid is important from those situations where counterflow does not occur or is not important.

Given the fact that under different conditions the same physical mechanism can cause a droplet or a bubble to move in opposite directions, it is appropriate to subdivide the situations terminologically. The earlier observations of bubble motion toward the *hotter regions* were called thermal Marangoni convection. It is reasonable to describe such a motion as a confined Marangoni convection or thermocapillarity. Motions toward the *colder regions*[4,5] can be described as an unconfined Marangoni convection. The present work deals with unconfined Marangoni convection.

This work demonstrates that small droplets are displaced along a fiber if a temperature gradient is created along the fiber. We show that the droplets move toward the cold region of the fiber and therefore this phenomenon can be attributed to the unconfined Marangoni convection according to the terminology proposed above. Only one work treating a comparable situation is known to the authors (Ref. 6). It considers two-dimensional drops in the framework of the lubrication approximation. The model of Ref. 6 assumes slip over the whole contact area between the drop and a supporting plane and neglects inertial effects. In Ref. 6 a detailed treatment of the flow patterns near the moving contact lines was given. A number of the assumptions adopted in Ref. 6 are restrictive or questionable and do not apply to the case of a single drop moving along a fiber. Also no experimental observation of the droplet motion was described there. Nevertheless, the general conclusion following from Ref. 6 is quite instructive: droplets can move towards the cold region. Such motion is supported by the present experiments and modeling of small droplets on nonuniformly heated fibers. We will show that a satisfactory description of droplet motion is based on the overall momentum balance. Details of the flow, near the moving contact lines between the droplet and the fiber, adjust themselves to the driving Marangoni stresses. This will allow us to develop a physical model of the phenomenon without detailed treatment of liquid motion inside a moving droplet. We also rule out the possibility that vapor recoil[7] creates sufficient thrust to propel the droplet toward the cold region of the fiber.

The mechanism of droplet motion revealed is of potential importance for a number of applications, in particular, for draining filters that coalesce liquid droplets from a gas stream.

The structure of this article is as follows. Section II contains a simplified model of droplet motion along a fiber due to unconfined Marangoni convection; Sec. III describes the

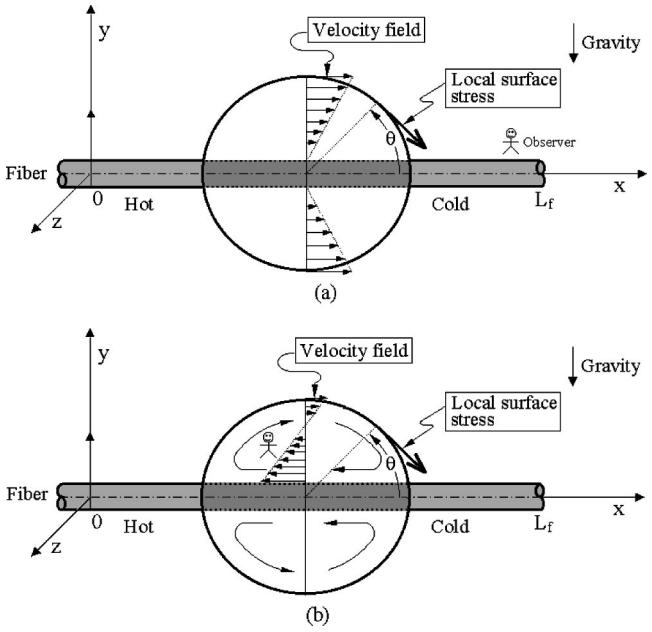

FIG. 1. Sketch of a spherical droplet on a fiber. (a) The flow field as perceived by an observer attached to the fiber. (b) The flow field as perceived by an observer moving with the center of the droplet.

temperature distribution in the fiber and droplet. Experimental observations are presented in Sec. IV, and are compared with the theory in Sec. V. The discussion is given in Sec. VI and the results are summarized in Sec. VII.

II. THERMALLY DRIVEN DROPLET MOTION

Consider a spherical droplet on a horizontal fiber shown in Fig. 1. At time $t<0$, we assume the fiber temperature, the temperature of the liquid, and that of the surrounding gas to be T_C. At time $t=0$ the fiber end at $x=0$ is instantaneously heated up to a higher temperature $T_H>T_C$. As a result, a transient temperature field along the fiber and in the droplet is established. Let $\Gamma=d\sigma/dT$ be the temperature coefficient of surface tension, with σ being the surface tension, T being temperature, and $\Gamma<0$. Then the local surface stress acting along the surface resulting from the Marangoni effect is given by $(\Gamma/\lambda)\partial T/\partial x$ as shown in Fig. 1. Temperature distribution over the droplet surface is discussed in detail in Sec. III; $\lambda=1/\sin\theta$ is the geometric factor, and the angle θ is the meridional angular spherical coordinate. The surface stress pulls liquid toward the cold end (Fig. 1), since both Γ and $\partial T/\partial x$ are negative, whereas λ is always positive.

The projection of the pulling stress along the fiber axis is given by

$$f=\Gamma\frac{\partial T}{\partial x}\sin^2\theta. \tag{1}$$

Integrating over the droplet surface, we obtain the total pulling force as

$$F_1=2\pi a^2\Gamma\overline{\frac{\partial T}{\partial x}}, \tag{2}$$

where a is the volume-equivalent droplet radius, and

$$\overline{\frac{\partial T}{\partial x}}=\int_0^\pi \sin^3\theta\frac{\partial T}{\partial x}d\theta \tag{3}$$

is calculated in Sec. III.

To calculate the friction force acting on the moving droplet, we assume, as the first approximation, that the flow field in the droplet is similar to that in a cylindrical layer pulled by the fiber [Fig. 1(b)]. This means that we assume that the flow is locally almost parallel to the fiber and satisfies the no-slip boundary condition $v_x=U$ at $R=a_f$ and $v_x=0$ at $R=a$. Here, v_x is the velocity of liquid motion along the fiber, R is the radial coordinate in the plane normal to the fiber axis, a is the volume-equivalent droplet radius, a_f is the fiber cross-sectional radius, and U is the velocity of the droplet center. The velocity profile is found as a solution of the Navier–Stokes equations in cylindrical coordinates subject to these boundary conditions, which yields the shear stress as

$$\mu\frac{dv_x}{dR}=-\frac{\mu U}{Rln(a/a_f)}, \tag{4}$$

where μ is the liquid viscosity. The shear stress acts over the fiber surface $4\pi a_f a$, which yields a friction force of the order of

$$F_2=-4\pi\mu a\frac{U}{ln(a/a_f)}. \tag{5}$$

It is emphasized that in the derivation of Eqs. (4) and (5) it was assumed that the shear stress at the fiber surface remains constant throughout the diameter of the drop. This assumption definitely does not hold in the vicinity of the moving contact lines at the leading and trailing edges of the drop. It is well known[6,8–11] that the long-range van der Waals interactions and local hydrodynamic effects result in the Navier–Maxwell slip boundary condition. In the vicinity of the contact lines, the slip condition replaces the one used to derive Eqs. (4) and (5) ($v_x=U$ at $R=a_f$). The slip eliminates a singularity at the moving contact lines at the edges of the drop. The size of the regions near the contact lines is of the order of ϵa, where $\epsilon=-1/ln(\bar{\lambda}/a)\ll 1$ ($\bar{\lambda}$ is a molecular slip coefficient, $\bar{\lambda}\ll a$). Since the shear stress at the edges is finite, whereas the corresponding area is $O(\epsilon)\ll 1$, the difference between the total shear force from the fiber acting on the drop, and F_2 of Eq. (5) is much smaller than F_2. As a result, F_2 presents a plausible estimate of the total shear force based on the observed velocity.

Combining the forces of Eqs. (2) and (5) in the equation of droplet motion, we obtain

$$\frac{4}{3}\pi a^3\rho_l\frac{dU}{dt}=2\pi a^2\Gamma\overline{\frac{\partial T}{\partial x}}-4\pi\mu a\frac{U}{ln(a/a_f)}, \tag{6}$$

where ρ_l is the liquid density, and t is time.

The latter equation is transformed to the form

$$\frac{dU}{dt}=\frac{3}{2}\frac{\Gamma}{\rho_l a}\overline{\frac{\partial T}{\partial x}}-\frac{3}{ln(a/a_f)}\frac{\nu}{a^2}U, \tag{7}$$

where kinematic viscosity of liquid is denoted by $\nu=\mu/\rho_l$.

Slight variation of the droplet volume-equivalent radius, a, due to evaporation is accounted for via the mass balance equation

$$\frac{da}{dt}=-E, \tag{8}$$

where the evaporation rate E is calculated in the Appendix [Eq. (A25)].

Equations (7) and (8) are supplemented by the kinematic relation

$$\frac{dX}{dt}=U, \tag{9}$$

with X being the x coordinate of the droplet center.

Equations (7)–(9) form a closed system describing droplet motion, given a known temperature gradient. The initial conditions are given by

$$t=0: \quad U=0, \tag{10a}$$

$$a=a_0, \tag{10b}$$

$$X=X_0, \tag{10c}$$

where a_0 and X_0 are the initial radius and position of the droplet. The initial condition for the temperature will be discussed [Eqs. (12) and (A27)].

III. TEMPERATURE DISTRIBUTION IN THE FIBER AND DROPLET

For a tiny droplet we assume that the temperature of liquid at a position x=constant is that of the fiber at this cross section. This assumption is plausible for smaller droplets. For bigger ones it will definitely be less accurate. Transient temperature distribution in a thin fiber is governed by the equation

$$\frac{\partial T_f}{\partial t}=\alpha_f\frac{\partial^2 T_f}{\partial x^2}-\frac{2h}{\rho_f c_f a_f}(T_f-T_C), \tag{11}$$

where T_f is the fiber temperature, ρ_f, c_f, and α_f are the density, specific heat, and thermal diffusivity of the fiber, respectively. Also h is the heat transfer coefficient at the lateral surface of the fiber.

The solution of Eq. (11) is subject to the following initial and boundary conditions:

$$t=0: \quad T_f=T_C, \tag{12a}$$

$$t>0: \quad \begin{cases} x=0, & T_f=T_H \\ x=L_f, & \dfrac{\partial T_f}{\partial x}=0, \end{cases} \tag{12b}$$

where L_f is the fiber length. Equation (12a) assumes that initially the fiber has a uniform temperature T_C.

A solution of Eqs. (11) and (12) is given in Ref. 12. In the present notation it reads

$$\frac{T_f-T_C}{T_H-T_C}=\frac{\cosh(\mathrm{Bi}^{1/2}x_1/b)}{\cosh(\mathrm{Bi}^{1/2}L_f/b)} -\sum_{n=1}^{\infty}(-1)^{n+1}\frac{2\mu_n}{\mu_n^2+\mathrm{Bi}(L_f/b)^2} \times\cos\left(\mu_n\frac{x_1}{L_f}\right)\exp[-(\mu_n^2+\mathrm{Bi}\,L_f^2/b^2)\mathrm{Fo}], \tag{13}$$

where

$$\mu_n=\frac{(2n-1)}{2}\pi, \tag{14a}$$

$$x_1=L_f-x, \tag{14b}$$

$$b=a_f/2, \tag{14c}$$

and the Biot and Fourier numbers are given by

$$\mathrm{Bi}=\frac{hb}{k_f}, \tag{15a}$$

$$\mathrm{Fo}=\frac{\alpha_f t}{L_f^2}, \tag{15b}$$

where the thermal conductivity of the fiber is denoted by k_f.

The temperature distribution Eq. (13) is used in Eq. (7) (with $T=T_f-\Delta T$) to calculate the temperature gradient $\overline{\partial T/\partial x}$. Note that ΔT expresses the effect of the evaporative cooling calculated in the Appendix [Eq. (A27)].

From Eq. (13) we find

$$\overline{\frac{\partial T}{\partial x}}=-(T_H-T_C)\left\{\frac{\mathrm{Bi}^{1/2}M_1}{b\cosh(\mathrm{Bi}^{1/2}L_f/b)} +\sum_{n=1}^{\infty}(-1)^{n+1}\frac{2\mu_n}{\mu_n^2+\mathrm{Bi}\,L_f^2/b^2}\left(\frac{\mu_n}{L_f}\right)N_n \times\exp\left[-\left(\mu_n^2+\mathrm{Bi}\frac{L_f^2}{b^2}\right)\mathrm{Fo}\right]\right\}, \tag{16}$$

where

$$M_1=\int_0^{\pi}\sin^3\theta\sinh\left[\mathrm{Bi}^{1/2}\frac{x_1(\theta)}{b}\right]d\theta, \tag{17a}$$

$$N_n=\int_0^{\pi}\sin^3\theta\sin\left[\mu_n\frac{x_1(\theta)}{L_f}\right]d\theta, \quad n=1,2,\ldots. \tag{17b}$$

$$x_1(\theta)=L_f-X-a\cos\theta. \tag{17c}$$

Lateral cooling of the fiber is due to the natural convection in air. For a fiber of $a_f=0.0060$ cm and the temperature difference $T_H-T_C=60\,^{\circ}\mathrm{C}$ the corresponding product of the Grashof (Gr) and Prandtl (Pr), numbers (needed to calculate the Nusselt number and the heat transfer coefficient) is $\mathrm{Gr}\,\mathrm{Pr}\approx 10^{-2}$. For such a value of the product, the Nusselt number $\mathrm{Nu}=h2a_f/k_a$ is about $10^{-0.2}$ for the natural convection from a horizontal cylinder, where k_a is the thermal conductivity of air (Ref. 13). Therefore,

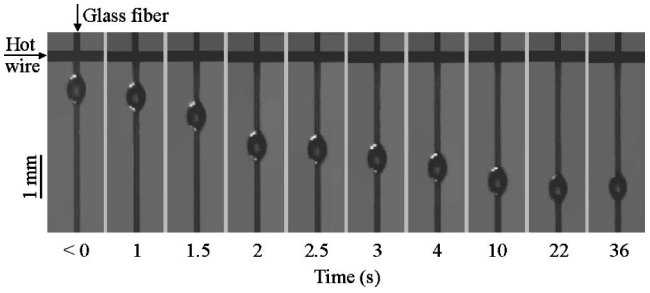

FIG. 2. Images of an *n*-decane droplet ($a_m = 0.22$ mm, $l = 0.72$ mm) at various times. Both the hot wire and glass fiber were in a horizontal plane; top view.

$$h = 0.631 \frac{k_a}{2a_f}, \tag{18}$$

where $0.631 = 10^{-0.2}$.

IV. EXPERIMENTAL OBSERVATIONS

Generatrices of the droplets seen on the photographs (for example, Fig. 2) are more nearly parabolic than circular. The apparent static and dynamic contact angles seen in the images are of the order of 60°. In the present case of a glass fiber, we are dealing with the case of partial wettability, with the London–van der Waals forces strong enough to stretch an initially spherical droplet into a paraboloidal body. Since the contact angles were significantly larger than zero, there is no question of perfect wettability, and no precursor film ahead of the liquid drop was assumed.

To estimate droplet sizes from the photographs, we approximated their shapes by a paraboloidal body of revolution:

$$r = -\frac{4}{l^2}(a_m - a_f)\xi^2 + a_m, \tag{19}$$

where the droplet surface meets the fiber at $\xi = \pm l/2$. The maximal droplet radius is a_m, and l is the length of the droplet along the fiber.

The droplet volume-equivalent radius a is defined as

$$\frac{4}{3}\pi a^3 = \int_{-l/2}^{l/2} \pi r^2 d\xi - \pi a_f^2 l, \tag{20}$$

which yields using Eq. (19):

$$a = [l(a_m - a_f)(2a_m + 3a_f)/5]^{1/3}. \tag{21}$$

Liquid viscosity μ is taken to be dependent on the temperature at the droplet center T_{cen} as[14]

$$\mu = \mu_0 \exp\left[3.8 T_b \left(\frac{1}{T_{\text{cen}}} - \frac{1}{T_0}\right)\right], \tag{22}$$

where μ_0 is the viscosity at some reference temperature T_0, and T_b is the boiling temperature.

Experiments were done with droplets of *n*-decane, *n*-undecane, *n*-dodecane, and *n*-hexadecane. The physical properties of these fluids are presented in Table I. It was assumed that *n*-decane evaporated by a perceptible amount, but evaporation of *n*-undecane, *n*-dodecane, and *n*-hexadecane was imperceptible.

In the experiments, an electrical current through a piece of nichrome wire (composed of 60% chromium, 16% nickel, and 24% iron) served as heating source. The heater wire ran horizontally along the z axis of Fig. 1 (normal to x and y axes), and touched the glass fiber at $x = 0$. The current through the wire was adjusted to control its temperature. A single silica glass fiber ($a_f = 0.060$ mm) was placed underneath the wire. The glass fiber was perpendicular to both the Earth's gravity and to the nichrome wire. The properties of the fiber are shown in Table II. Droplets, of various sizes (listed in Table III), of *n*-decane, *n*-undecane, *n*-dodecane, and *n*-hexadecane were deposited on the fiber, near the position where the hot wire crossed the fiber. In each of the experiments there was a single droplet on the fiber. The pa-

TABLE I. Physical properties of *n*-decane, *n*-undecane, *n*-dodecane, and *n*-hexadecane at $T_0 = 20\,^\circ$C (293 K). A_*, B_*, and C_* are the parameters of the Antoine equation (A20) in the Appendix (see Refs. 15–17).

Parameter	*n*-decane	*n*-undecane	*n*-dodecane	*n*-hexadecane
Molecular mass, M_v, g/mol	142.28	156.31	170.34	226.45
Density, ρ_l, g/cm^3	0.73	0.74	0.7491	0.773
Temperature coefficient of surface tension, Γ, g/(s^2 K)	−0.0919	−0.0894	−0.0879	−0.0843
Viscosity at 293 K, μ_0, g/cm s	0.907×10^{-2}	1.182×10^{-2}	1.492×10^{-2}	3.4512×10^{-2}
Boiling point, T_b, K	447.15	469.13	489.43	560.2
Latent heat of evaporation, I_v, kJ/kg	351			
Specific heat, c_p, kJ/(kg K)	2.28			
Diffusion coefficient of vapor in air, D, cm^2/s	0.057 349			
A_*	16.0114			
B_*	3456.8			
C_*	−78.67			

TABLE II. Properties of the silica glass fiber as given by the manufacturer.

Parameter	Value
Cross-sectional radius, a_f, mm	0.060
Length, L_f, mm	20
Density, ρ_f, g/cm^3	2.21
Specific heat, c_f, cal/(g K)	0.184
Thermal conductivity, k_f, kcal/(m hr K)	0.877
Thermal diffusivity, α_f, cm^2/s	0.006

rameters of the droplets are given in Table III. When the nichrome wire was heated to T_H, (~80 °C, 353 K), the motion of the droplet was observed through an optical microscope. The surrounding air temperature, T_C, was ~20 °C, 293 K. Images were taken through an optical microscope at 30 frames per second by a video camera.

Figure 2 shows images of the *n*-decane droplet when $t<0$, and $t=1$, 1.5, 2–36 s after the wire was heated. The droplet moved along the fiber. The movement was from the top to bottom in the figure, but in a horizontal plane in the experiment, to minimize the effect of gravity on the motion, after the hot wire has begun to heat the glass fiber at $t=0$. The movement of the droplet occurred during the first 3 or 4 s after the wire was heated (Figs. 4–7).

V. COMPARISON WITH THE THEORY

Figure 3 shows the volume-equivalent radii of a large droplet (0.0616 mm^3 in volume) and a small droplet (0.0181 mm^3 in volume) of *n*-decane versus time. The droplets are referred to as ''large'' and ''small'' according to Table III. For example, the large *n*-decane droplet is the one corresponding to the first line in Table III, and so on. The volume loss at $t=35$ s was 67.5% and 28.6% for the small and large drops of Fig. 3, respectively. The volume decreased at a higher rate than predicted from the theory [Eq. (A25)]. Calculations indicate that the evaporation rate is not high enough to be entirely responsible for the reduction in droplet size seen in experiments.

It is easy to show that the discrepancy between the predicted and measured rate of decrease of the droplet size cannot be attributed to the enhancement of evaporation rate near a curved surface (the Kelvin effect). Indeed, the Kelvin effect results in a rise of vapor pressure near a curved surface, where evaporation proceeds easier than near a plane surface, as per

TABLE III. Droplet parameters.

Droplet		a_m (mm)	l (mm)	X_0 (mm)
n-decane	large	0.22	0.72	0.64
	small	0.15	0.50	0.54
n-undecane	large	0.29	0.84	0.97
	small	0.15	0.48	0.55
n-dodecane	large	0.31	0.94	0.77
	small	0.16	0.52	0.58
n-hexadecane	large	0.26	0.75	0.49
	small	0.16	0.47	0.43

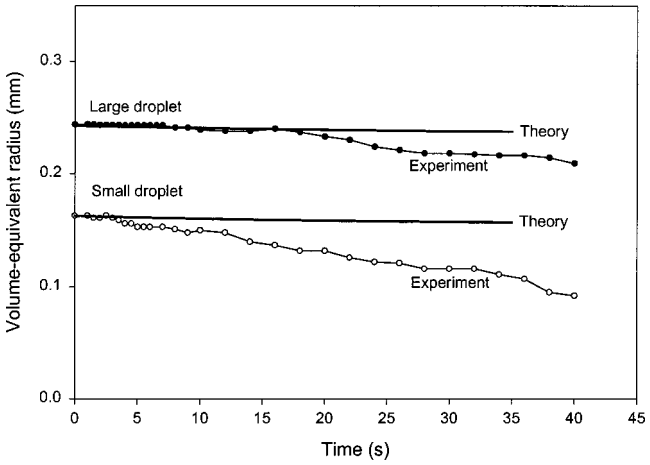

FIG. 3. Volume-equivalent radii of large and small *n*-decane droplets.

$$p_{\mathrm{sat,cur}}=p_{\mathrm{sat}}\left(1+\frac{\omega}{kT}\frac{2\sigma}{a_m}\right), \tag{23}$$

where $p_{\mathrm{sat,cur}}$ is the vapor pressure near the curved droplet surface, p_{sat} is the vapor pressure near a plane surface, ω is the volume per one molecule in liquid state, k is the Boltzmann's constant, T is the temperature, σ is the surface tension coefficient, and a_m is the radius of curvature; the volume $\omega=M_v/(\rho_l N_A)$, where N_A is the Avogadro's number. For *n*-decane, given the values of M_v and ρ_l in Table I and $N_A=6.025\times10^{23}\,\mathrm{mol}^{-1}$, we find $\omega=0.32\times10^{-21}\,\mathrm{cm}^3$. For the estimate we take $a_m=10^{-2}$ cm and $T=300$ K. The surface tension of *n*-decane $\sigma=23.2$ g/s^2 at this temperature; also $k=1.38\times10^{-16}\,\mathrm{g\,cm^2/(s^2\,K)}$. Then for *n*-decane the ratio

$$\frac{\omega}{kT}\frac{2\sigma}{a_m}=3.59\times10^{-5}, \tag{24}$$

which is negligibly small compared to one, and therefore has no effect in Eq. (23). This means that these droplets are too large for Kelvin effect to be significant, and $p_{\mathrm{sat,cur}}\approx p_{\mathrm{sat}}$. As a result, the rate of droplet evaporation given by Eq. (A25) is practically unaffected in the present case by droplet curvature.

Formation of a thin and unstable liquid film on the fiber during droplet motion is a plausible reason for the radius reduction observed in the experiments (Fig. 3). In the case of partial wettability that we are dealing with, this invisible film should break up into a succession of still invisible tiny droplets. The decrease in droplet diameter corresponding to the images from 22 to 36 s in Fig. 2 shows that the diameter decreased, after the motion stopped, more rapidly than calculated [Eq. (A25)] by the evaporation rate theory. This discrepancy suggests inaccuracies in the values of the parameters A_*, B_*, and C_* of the Antoine equation (see Table I). For *n*-undecane, *n*-dodecane, and *n*-hexadecane, no variations of droplet radii during experiments were detected.

Figures 4–7 show the positions of *n*-decane, *n*-undecane, *n*-dodecane, and *n*-hexadecane droplets versus time, compared to the theoretical results of numerical solution of Eqs. (7)–(9). It is seen that qualitatively the theory

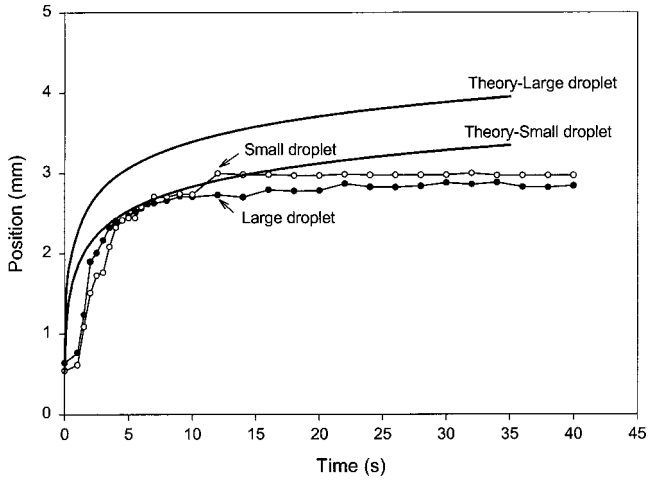

FIG. 4. Positions of large and small *n*-decane droplets as a function of time.

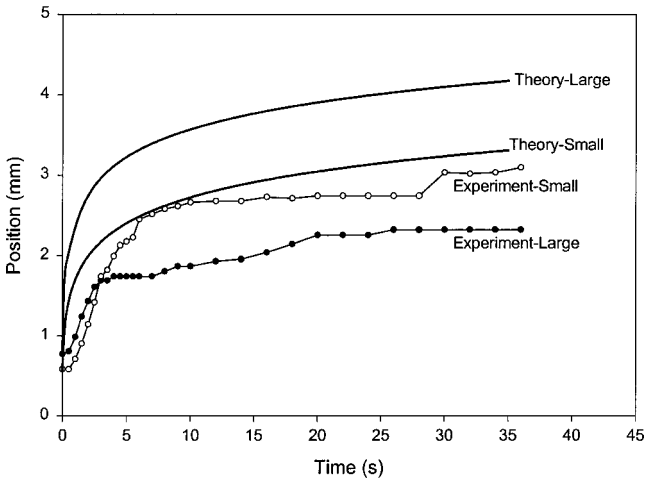

FIG. 6. Positions of large and small *n*-dodecane droplets as a function of time.

reproduces the main trend found experimentally: *all the droplets move toward the cold region of the fiber*. This conclusion agrees with the predictions of Ref. 6. On the other hand, the direction of droplet motion is opposite to that described in Refs. 2 and 3, as discussed in Sec. I. The quantitative agreement of the calculated and observed displacement as a function of time is reasonable, given the simplifications used in the theoretical model.

Some minor effects were missed by the theoretical predictions. In the experiments a smaller droplet moved further than a larger one: in Fig. 4, by 4.4%, Fig. 5, by 22%, Fig. 6, by 23.4%, and in Fig. 7, by 23.5%. In the theory the bigger droplet moved further. The reason for this discrepancy may be in the assumption that liquid in the droplet has the same temperature as the fiber at the same cross section. In reality the bigger droplets may be significantly cooler in the regions farthest from the fiber. Then their motion should be slower than the theory predicts. In Figs. 4–7, the experimental curves show the random stick–slip motions of the droplets.

VI. DISCUSSION

Droplet velocity achieves its maximal value very soon after the heating of the fiber begins at $t=0$ and $x=0$. Then the velocity decreases rapidly. The results shown in Figs. 4–7 imply that droplet displacement takes place for about 5 s; after that the droplets practically stop. It is very instructive, however, to see that the smallest droplets can be moved by the temperature gradient to a distance which is more than ten times larger than their initial volume-equivalent radius. The interval of time during which droplets move roughly corresponds to the time during which the section of the temperature profile in the fiber possessing the highest temperature gradients passes the droplet. A rough estimate of the time interval, t_*, can be obtained using the results for a transient heat flow in a semi-infinite body (Ref. 13, pp. 136–137). The corresponding solution, being much simpler than the present one given by Eq. (13), nevertheless shows the same trend, thus we obtain $t_* \approx (l+X_0)^2/\alpha_f$. Taking for the estimate $l=X_0=0.06\,\mathrm{cm}$ and $\alpha_f=0.006\,\mathrm{cm}^2/\mathrm{s}$ (Tables II and III), we obtain $t_*=2.4\,\mathrm{s}$. After the highest temperature gra-

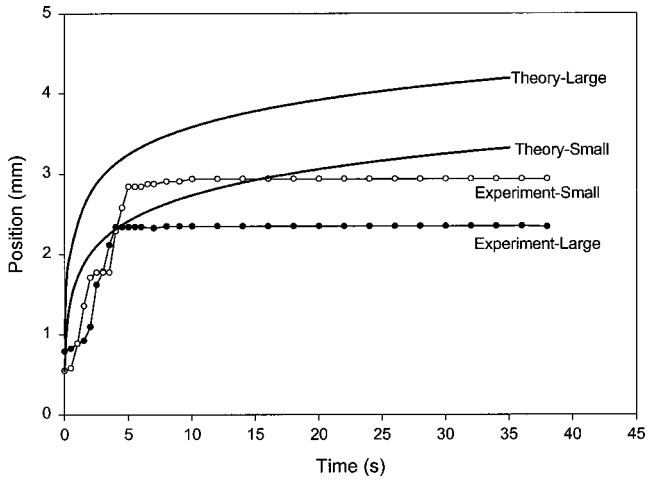

FIG. 5. Positions of large and small *n*-undecane droplets as a function of time.

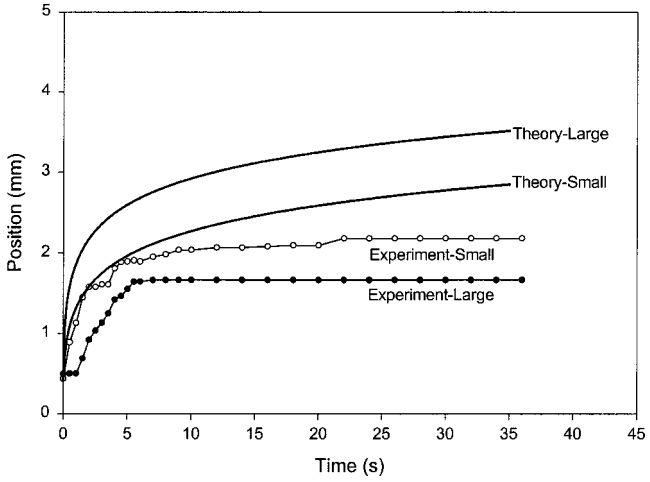

FIG. 7. Positions of large and small *n*-hexadecane droplets as a function of time.

dients passed, the droplet finds itself in an almost isothermal environment, where the temperature gradients and expected motion are small.

It is emphasized that the mechanism of the droplet motion we are dealing with should not depend on the fiber material. To check this, we placed a copper wire parallel to the glass fiber in a separate series of the experiments. The cross-sectional radius of the copper wire was $a_w = 0.077$ mm, and *n*-undecane drops similar to those of Fig. 5 were placed on it. The glass fiber and a parallel copper wire were heated up by the same heating wire. We found that the droplets moved on both the glass fiber and the copper wire. The droplet on the glass fiber always moved a shorter distance and responded more slowly. Droplets on the copper wire moved to distances of the order of several millimeters which were not too different from the values measured on the glass fiber.

The fact that the delay time is shorter on the copper wire is certainly related to the fact that the thermal diffusivity of copper, $\alpha_c = 1.12\ \mathrm{cm}^2/\mathrm{s}$, is much higher than that of the glass $\alpha_f = 0.006\ \mathrm{cm}^2/\mathrm{s}$. Therefore, the delay time on the copper wire $t_{\mathrm{dc}} = X_0^2/\alpha_c$ is much less than the delay time on the glass fiber. However, the effect of the heating up of the droplet itself, which takes time of the order of l^2/α_l should also be accounted for in the case of the droplets on the copper wire ($\alpha_l = 0.000\,86\ \mathrm{cm}^2/\mathrm{s}$ is the thermal diffusivity of the liquid, *n*-undecane). Since α_l and $\alpha_f \ll \alpha_c$ and l is of the order of X_0, we find that $X_0^2/\alpha_c \ll l^2/\alpha_l$ and l^2/α_l is of the order of X_0^2/α_f. Then the total delay time on the copper wire is mostly determined by the time of the droplet heating up. As a result, the delay times on the copper wire and on the glass fiber were not too different.

Similar droplet motions were observed for other fluids such as transmission oil, lubrication oil, and vegetable oil on a 16 μm-Kevlar® fiber. For the sake of brevity, and due to the fact that the physical properties of the oils were not known to the extent needed for the calculations (Table I), the corresponding details are omitted here.

Vapor outwardflowing from a liquid surface exerts a thrust force on it, which is termed vapor recoil (Ref. 7 and the Appendix). It is emphasized that vapor recoil cannot be responsible for the observed effect. The peak value of the thrust force on the droplet, toward the cooler region of the fiber, due to the vapor recoil effect, appears to be of the order of $P \simeq 10^{-8}$ dyne (the Appendix). Figures 4–7 show that the droplet velocity is of the order of $U \simeq 10^{-2}$ cm/s. For the first 10 s, the observed acceleration of the droplet dU/dt is about $10^{-3}\ \mathrm{cm/s}^2$. Therefore for $a \approx 10^{-2}$ cm, the inertial force associated with the observed motion of the droplet is of the order of $\rho_l (4/3)\pi a^3 dU/dt \approx 10^{-9}$ dyne (ρ_l is the liquid density). The inertial force can be neglected because it is even smaller than the slight thrust resulting from vapor recoil. If vapor recoil were the driving force instead of the thermocapillary force, vapor recoil should be balanced only by the viscous drag, the magnitude of which is of the order of

$$F_D = C\mu a U, \tag{25}$$

for a creeping flow, where $U \approx 10^{-2}$ cm/s, $a \approx 10^{-2}$ cm, $\nu \simeq 10^{-2}\ \mathrm{cm}^2/\mathrm{s}$, and the Reynolds number $\mathrm{Re} \approx 10^{-2}$. In Eq. (25) C is a dimensionless constant. If vapor recoil was responsible for the droplet motion, then the dimensionless coefficient from Eq. (25) should be equal to

$$C = \frac{P}{\mu a U}. \tag{26}$$

Assuming $\mu \approx 10^{-2}\ \mathrm{g/(cm\,s)}$, $a \simeq 10^{-2}$ cm, $U \approx 10^{-2}$ cm/s, and $P \approx 10^{-8}$ dyne, Eq. (26) yields $C \simeq 10^{-2}$, whereas one expects a much higher value of C (of the order of one) for a creeping flow of this kind. Indeed, in the kindred problems on solid, liquid, or gaseous spheres slowly moving in viscous fluid, the range of C is $4\pi \leqslant C \leqslant 6\pi$, which follows from the Stokes law and the Hadamard–Rybczynski formula.[18] According to Eq. (5) $C = 4\pi/ln(a/a_f) \approx 4\pi/ln\ 10 = 5.46$. If the value of $C \simeq 10^{-2}$ is true, the gravitational slip of a tiny droplet down a vertical fiber under the action of the gravitational force, $F_g = g\rho_l (4/3)\pi a^3 \simeq 10^{-3}$ dyne, would proceed with a velocity $U = F_g/(C\mu a) \approx 10^3$ cm/s, which was not observed. Therefore, vapor recoil can be discarded as a driving force for the droplet motion. Then the most credible source of the droplet motion is the unconfined thermocapillary Marangoni convection.

According to the photographs of Fig. 2, the shape of the droplet does not change significantly during its motion, which means that the paraboloidal approximation of Eq. (19) holds all the time. This observation has the following explanation: the apparent advancing contact angle γ_a is related to its static counterpart $\gamma_{a,st}$ via Hoffman's law[6,19]

$$\gamma_a = \gamma_{a,st} + 4.54\,\mathrm{Ca}^{1/3}, \tag{27}$$

where the capillary number $\mathrm{Ca} = U\mu/\sigma$ representing the dimensionless rate of the contact line motion, should be much smaller than one. In the present case of $U \approx 10^{-2}$ cm/s, $\mu \approx 10^{-2}\ \mathrm{g/(cm\,s)}$ and $\sigma = 23.2\ \mathrm{g/s}^2$, $\mathrm{Ca} = 4.3 \times 10^{-6} \ll 1$. From Eq. (27) we obtain $\gamma_a - \gamma_{a,st} = 7.4 \times 10^{-2}$, which corresponds to the difference between the dynamic and static apparent contact angles of only about 4°. This explains why the droplet shape hardly changes during its motion along the fiber.

VII. SUMMARY

Tiny droplets begin to move along a fiber when one end of the fiber is suddenly heated. The motion of the droplet is always directed toward the cold region, and is opposite to the motion expected from the confined Marangoni convection of Refs. 2 and 3. These observations are similar to the unconfined thermocapillary Marangoni convection demonstrated for thin liquid films in Refs. 4 and 5. In the present experiments tiny droplets were displaced to a distance ten times their radii in about 10 s.

ACKNOWLEDGMENTS

This research was partially supported by the National Science Foundation in Grant Nos. CTS-9900949, ''Nanofibers in Coalescer Filter Media'' and DMI-9813098, ''Manufacturing of Polymer Nanofibers by Electrospinning.'' Support also came from the Coalescence Research Consortium

of the University of Akron. The assistance of Dr. Dan Galehouse with the design of the experiments is greatly appreciated.

APPENDIX: DROPLET EVAPORATION AND VAPOR RECOIL

To estimate the evaporation rate and vapor recoil rate we consider the case of a spherically symmetric droplet. First, we shall find a local relation between the pressure at the liquid side of the interface and vapor density near it. Then we shall introduce the effect of a nonuniform temperature distribution leading to an overall thrust force acting on the droplet. We assume that liquid vapor and air are the only substances in contact with droplet surface. Then the continuity equation and the conservation equations for vapor and air read[20]

$$\frac{d}{dr}(\rho v_r r^2)=0, \tag{A1a}$$

$$\frac{d}{dr}(\rho v_r r^2 Y_v)=\frac{d}{dr}\left(\rho D r^2 \frac{dY_v}{dr}\right), \tag{A1b}$$

$$\frac{d}{dr}(\rho v_r r^2 Y_a)=\frac{d}{dr}\left(\rho D r^2 \frac{dY_a}{dr}\right), \tag{A1c}$$

where ρ is the density of the mixture of vapor and air, v_r is the radial velocity of the mixture, r is the radial coordinate, D the diffusion coefficient, and Y_v and Y_a the mass fractions of vapor and air, respectively.

Integrating Eqs. (A1), we obtain

$$\rho v_r r^2=\frac{\dot{m}}{4\pi}, \tag{A2a}$$

$$\frac{\dot{m}}{4\pi}Y_v-\rho D r^2 \frac{dY_v}{dr}=\frac{\dot{m}}{4\pi}, \tag{A2b}$$

$$\frac{\dot{m}}{4\pi}Y_a-\rho D r^2 \frac{dY_a}{dr}=0, \tag{A2c}$$

where the constants of integration were found using the fact that the droplet surface is permeable for liquid vapor only, and $\dot{m}$ is the total mass flux from the whole droplet surface.

Solving the differential Eq. (A2b) with the boundary condition

$$r=\infty, \quad Y_v=Y_{v\infty}, \tag{A3}$$

where $Y_{v\infty}$ is the mass fraction of vapor at infinity, we obtain

$$Y_v=1-(1-Y_{v\infty})\exp\left(-\frac{\dot{m}}{4\pi\rho D r}\right). \tag{A4}$$

At the droplet surface $r=a$ (a is the droplet radius) the mass fraction of vapor is equal to the saturation value (described below) Y_{vs}, which allows us to find from Eq. (A4) the total mass flux $\dot{m}$ as in Ref. 20:

$$\dot{m}=4\pi\rho\,\mathrm{Da}\,ln(1+B), \tag{A5}$$

where

$$B=\frac{Y_{vs}-Y_{v\infty}}{1-Y_{vs}} \tag{A6}$$

is the Spalding transfer number.

Expressions (A5) and (A6) can also be obtained from Eq. (A2c) given the fact that

$$Y_v+Y_a=1. \tag{A7}$$

Using Eqs. (A2b), (A5), and (A6), we find the mass flux of the vapor at the droplet surface, $j=-\rho D(dY_v/dr)|_{r=a}$, as

$$j=\rho h_m(Y_{vs}-Y_{v\infty}), \tag{A8a}$$

$$h_m=\frac{D}{a}\frac{ln(1+B)}{B}, \tag{A8b}$$

where h_m is the mass transfer coefficient.

The corresponding Sherwood number reads[20]

$$\mathrm{Sh}=\frac{h_m 2a}{D}=2\frac{ln(1+B)}{B}. \tag{A9}$$

The momentum balance at the droplet surface is given by

$$p+\rho v_r^2=p_l+\rho_l v_l^2, \tag{A10}$$

where p and p_l are the pressures on the vapor/air and liquid sides, respectively, ρ_l is the liquid density, and v_l is the velocity of the surface motion relative to the liquid.

Due to the mass conservation of liquid and its vapor

$$\rho_l v_l=\left(\rho v_r Y_v-\rho D\frac{dY_v}{dr}\right)\Big|_{r=a}, \tag{A11}$$

and thus, using Eqs. (A2a), (A2b), and (A5), we find

$$\rho_l v_l=\frac{\dot{m}}{4\pi a^2}=\rho\frac{D}{a}ln(1+B). \tag{A12}$$

Also, from Eqs. (A2a) and (A5)

$$\rho v_r|_{r=a}=\rho\frac{D}{a}ln(1+B). \tag{A13}$$

Substituting Eqs. (A12) and (A13) in Eq. (A10), we obtain

$$p+\rho\left(\frac{D}{a}\right)^2 ln^2(1+B)=p_l+\frac{\rho}{\rho_l}\rho\left(\frac{D}{a}\right)^2 ln^2(1+B). \tag{A14}$$

Since the ratio $\rho/\rho_l \ll 1$, we can neglect the last term in Eq. (A14), and find

$$p_l=p+\rho\left(\frac{D}{a}\right)^2 ln^2(1+B). \tag{A15}$$

Typically, $Y_{v\infty}=0$ (no vapor far from the droplet), and $Y_{vs} \ll 1$, which allows one to reduce Eq. (A15), using Eq. (A6), to the following form:

$$p_l=p+\frac{c_{vs}^2}{\rho}\left(\frac{D}{a}\right)^2, \tag{A16}$$

where the vapor density $c_{vs}=\rho Y_{vs}$, and the Stefan flux[20] at the droplet surface is neglected.

The vapor density c_{vs} at the surface depends on the surface temperature of the droplet. Since in the present case the temperature distribution is expected to be nonuniform over the droplet surface, the last term in Eq. (A16) will be responsible for the thrust applied to the droplet due to vapor recoil.

The contribution of the first term on the right-hand side in Eq. (A16) will be zero, since the total pressure p is uniform over the droplet surface.

The magnitude of the thrust P is given by

$$P=\left|-2\pi a^2\int_0^{\pi} p_l n_x \sin\theta d\theta\right|, \tag{A17}$$

where $n_x=\cos\theta$ is the projection of the outer unit normal to the surface onto the axis of the tiny fiber supporting the droplet, and θ is the meridional angular spherical coordinate.

From the equation of state of the vapor, its density is given by

$$c_{vs}=\frac{p_{\mathrm{sat}}M_v}{R_gT}, \tag{A18}$$

where $p_{\mathrm{sat}}(T)$ is the saturation pressure of the vapor at the surface temperature T, M_v is the molecular mass of the vapor, and R_g is the absolute gas constant.

Substituting Eqs. (A16) and (A18) in Eq. (A17), we arrive at

$$P=\left|-\frac{2\pi}{\rho}\left(\frac{DM_v}{R_g}\right)^2\int_0^{\pi}\left(\frac{p_{\mathrm{sat}}(T)}{T}\right)^2\sin\theta\cos\theta d\theta\right|. \tag{A19}$$

The saturation pressure of several liquids is given as a function of the temperature by the Antoine equation[15]

$$p_{\mathrm{sat}}=0.001\,333\,224\exp\left(A_*-\frac{B_*}{T+C_*}\right), \tag{A20}$$

where p_{sat} is given in bar ($1\ \mathrm{bar}=10^5\ \mathrm{N\,m^{-2}}$), and T is taken in degrees Kelvin. The values of the parameters A_*, B_*, and C_* for n-decane are shown in Table I.

For tiny droplets on tiny fibers we expect that droplet surface temperature is close to that of the fiber at a given cross section, and thus the thrust given by Eq. (A19) takes the form

$$P=\frac{2\pi}{\rho}\left(\frac{DM_v}{R_g}\right)^2\int_{-1}^{1}\left(\frac{p_{\mathrm{sat}}(T)}{T}\right)^2\xi d\xi, \tag{A21a}$$

$$\xi=\frac{X-x}{a}, \tag{A21b}$$

with $T=T_f-\Delta T$, where ΔT is discussed below [Eq. (A27)].

Decrease of the droplet volume-equivalent radius and droplet cooling due to evaporation should be accounted for to describe the droplet motion. In the limit of a small Spalding number $B\ll 1$, where $Y_{vs}\ll 1$, the mass transfer coefficient given by Eq. (A8b) reduces to

$$h_m=\frac{D}{a}. \tag{A22}$$

Therefore the mass flux of vapor (for n-decane $Y_{v\infty}=0$) according to Eqs. (A8a), (A18), and (A22) is given by

$$j=\rho\frac{D}{a}Y_{vs}=\frac{D}{a}c_{vs}=\frac{DM_v}{R_ga}\frac{p_{\mathrm{sat}}(T)}{T}. \tag{A23}$$

Integrating Eq. (A23) over the droplet surface, we obtain the mass balance equation for the droplet in the following form

$$\frac{d}{dt}\left(\rho_l\frac{4}{3}\pi a^3\right)=-\frac{DM_v}{R_ga}2\pi a^2\int_0^{\pi}\frac{p_{\mathrm{sat}}(T)}{T}\sin\theta\,d\theta, \tag{A24}$$

which reduces to the equation describing the volume-equivalent droplet radius

$$\frac{da}{dt}=-\frac{DM_v}{2\rho_lR_ga}\int_{-1}^{1}\frac{p_{\mathrm{sat}}(T)}{T}d\xi, \tag{A25}$$

defining E in Eq. (8). Here, as before, $p_{\mathrm{sat}}(T)$ is given by the Antoine equation (A20).

Temperature in a droplet cross-section T will be reduced as compared to the corresponding value of T_f due to the evaporation cooling. The relevant thermal balance reads

$$\frac{d}{dt}\left(\rho_lc_pT_{\mathrm{cen}}\frac{4}{3}\pi a^3\right)=c_pT_{\mathrm{cen}}\frac{d}{dt}\left(\rho_l\frac{4}{3}\pi a^3\right)+I_v\frac{d}{dt}\left(\rho_l\frac{4}{3}\pi a^3\right). \tag{A26}$$

Here I_v is the latent heat of evaporation, c_p is the specific heat of the liquid, and $T_{\mathrm{cen}}=T|_{\xi=0}$.

The term on the left-hand side of Eq. (A26) implies the general decrease of the droplet energy, whereas the two terms on the right-hand side describe two sources of energy decrease: convective losses due to vapor outflow, and evaporation cooling, respectively.

Equation (A26) can be integrated, which yields the reduction of the droplet temperature as compared to T_f by the following value:

$$\Delta T=T_{\mathrm{cen},0}-T_{\mathrm{cen}}=\frac{I_v}{c_p}ln\left(\frac{a_0}{a}\right)^3, \tag{A27}$$

where $T_{\mathrm{cen},0}$ and a_0 are the values of the temperature and radius without evaporation being accounted for.

[1] D. Quere, Annu. Rev. Fluid Mech. **31**, 347 (1999).
[2] N. O. Young, J. S. Goldstein, and M. J. Block, J. Fluid Mech. **6**, 350 (1959).
[3] R. S. Subramanian, in *Transport Processes in Bubbles, Drops and Particles*, edited by R. P. Chhabra and D. De Kee (Hemisphere, New York, 1990), pp. 1–42 and references therein.
[4] V. Ludviksson and E. N. Lightfoot, AIChE J. **17**, 1166 (1971).
[5] D. E. Kataoka and S. M. Troian, Nature (London) **402**, 794 (1999).
[6] M. C. Smith, J. Fluid Mech. **294**, 209 (1995).
[7] H. J. Palmer, J. Fluid Mech. **75**, 487 (1976), and references therein.
[8] E. B. Dussan V, Annu. Rev. Fluid Mech. **11**, 371 (1979).
[9] L. M. Hocking, Quarterly J. Mech. Appl. Math. **36**, 55 (1983).
[10] R. G. Cox, J. Fluid Mech. **168**, 169 (1986).
[11] P. G. de Gennes, X. Hua, and P. Levinson, J. Fluid Mech. **212**, 55 (1990).
[12] A. V. Luikov, *Analytical Heat Diffusion Theory* (Academic, New York, 1968).
[13] J. P. Holman, *Heat Transfer*, 7th ed. (McGraw-Hill, London, 1992).
[14] J. O. Hirschfelder, Ch. F. Curtiss, and R. B. Bird, *Molecular Theory of Gases and Liquids* (Wiley, New York, 1954).
[15] R. C. Reid, J. M. Prausnitz, and B. E. Poling, *The Properties of Gases and Liquids* (McGraw-Hill, New York, 1987).
[16] E. N. Fuller, P. D. Schettler, and J. C. Giddings, Ind. Eng. Chem. **58**, 18 (1966).
[17] N. B. Vargaftik, Y. K. Vinogradov, and V. S. Yargin, *Handbook of Physical*

Properties of Liquids and Gases: Pure Substances and Mixtures, 3rd ed. (Begell House, New York, 1996).
[18] S. Kim and S. J. Karrila, *Microhydrodynamics* (Butterworth-Heinemann, Boston, 1991).
[19] S. F. Kistler, in *Wettability*, edited by J. C. Berg (Marcel Dekker, New York, 1993), pp. 311–429 and references therein.
[20] W. A. Sirignano, *Fluid Dynamics and Transport of Droplets and Sprays* (Cambridge University Press, Cambridge, 1999).